Dynamics of mantle flow and melting at a ridge-centered hotspot: Iceland and the Mid-Atlantic Ridge

Garrett Ito [a,*], Jian Lin [b,1], Carl W. Gable [c,2]

[a] *MIT / WHOI Joint Program, Department of Geology and Geophysics, Woods Hole Oceanographic Institution, Woods Hole, MA 02543, USA*

[b] *Department of Geology and Geophysics, Woods Hole Oceanographic Institution, Woods Hole, MA 02543, USA*

[c] *Earth and Environmental Sciences, Los Alamos National Laboratories, Los Alamos, NM 87545, USA*

Abstract

The dynamics of mantle flow and melting of a ridge-centered plume were investigated with three-dimensional variable-viscosity numerical models, focusing on three buoyancy sources: temperature, melt depletion, and melt retention. The width, W, to which a plume spreads along a ridge axis, depends on plume volume flux, Q, full spreading rate, U, buoyancy number, B, and ambient/plume viscosity contrast γ. When all melting effects are considered, our numerical results are best parameterized by $W = 2.37(Q/U)^{1/2}(B\gamma)^{0.04}$. Thermal buoyancy is first-order in controlling along-axis plume spreading while latent heat loss due to melting, and depletion and retention buoyancy forces contribute second-order effects. We propose two end-member models for the Iceland plume beneath the Mid-Atlantic Ridge (MAR). The first has a broad plume source with temperature anomaly ΔT_p of 75°C, radius, a, of 300 km, and Q of 1.2×10^7 km³/my. The second is of a narrower and hotter plume source with ΔT_p of 170°C, a radius of 60 km, and Q of 2.1×10^6 km³/my. The broad plume source predicts successfully the observed seismic crustal thickness, topographic, and gravity anomalies along the MAR, but predicts an along-axis geochemical plume width substantially broader than that suggested by the observed ^{87}Sr/^{86}Sr anomaly. The narrow plume source model predicts successfully the total excess crustal production rate along the MAR (2.5×10^5 km³/my) and a geochemical width consistent with that of the ^{87}Sr/^{86}Sr anomaly, but it requires substantial along-axis melt transport to explain the observed along-axis variations in crustal thickness, bathymetry, and gravity. Calculations suggest that lateral plume dispersion may be radially symmetric rather than channelled along the ridge axis and that the topographic swell, which is elongated along the Reykjanes Ridge, may be due to rapid off-axis subsidence associated with lithospheric cooling superimposed on a broader hotspot swell. The two plume source models predict seismic P-wave velocity reductions of 0.5–2% in the center of the plume, producing travel time delays of 0.2–1.2 s. Predicted P-wave delay times for the narrow plume source model are more consistent with recent seismic observations beneath Iceland, suggesting that this model may be more representative of the Iceland plume.

---

* Corresponding author. Fax: +1 508 457 2187. E-mail: gito@magellan.whoi.edu

[1] Tel: +1 508 289 2576. Fax: +1 508 457 2187. E-mail: jlin@whoi.edu.

[2] Tel: +1 505 665 3533. E-mail: gable@lanl.gov.

1. Introduction

Centered on the Mid-Atlantic Ridge (MAR), the Iceland hotspot is the largest melt anomaly throughout the world's mid-ocean ridge system and is among the large oceanic igneous provinces [1]. The idea that Iceland marks a mantle convection plume rising beneath the MAR has become well established since its original conception in the early 1970s (e.g. [2–4]). The broad topographic swell (Fig. 1) and correlated along-spreading-axis geochemical anomalies indicate that the plume rises beneath Iceland and spreads laterally along the ridge axis [4,5]. Such along-axis spreading of a mantle plume feeding a ridge axis may also explain topographic and geochemical anomalies affected by other near ridge-axis hotspots (e.g. [6–8]), many of which may have contributed substantially to the earth's heat and magmatic budget throughout geologic history.

While the original concept that plumes feed and spread along nearby ridges was proposed two decades ago, only recently have the fluid dynamic aspects been investigated quantitatively. Recent numerical and laboratory tank experiments have shown that the width, W, over which a plume spreads along axis, increases with plume volume flux, Q, and decreases with plate full-spreading rate, U [9–11]. Such studies are important in revealing the pertinent physical processes governing plume–ridge interactions and in placing theoretical constraints on properties of mantle plumes such as temperature anomaly, size and volume flux.

Two potentially important sources of buoyancy, however, have not been considered in previous plume–ridge studies. These are melt depletion, which lowers the Fe/Mg ratio in the residual mantle and thus reduces its density [12], and melt retention in the mantle, which also reduces mantle bulk density (e.g. [13–15]). It has been proposed that melt depletion may be primary in driving spreading of intraplate plumes beneath the lithosphere [16]. It has also been proposed that both melt retention buoyancy and depletion buoyancy may contribute significantly to along-axis variations in mantle flow and crustal thickness beneath normal mid-ocean ridges [17,18].

The objectives of this study were two-fold. First, we investigated numerically the effects of thermal and melting related buoyancy forces on along-axis spreading of ridge-centered plumes. We used three-dimensional (3D), variable viscosity, numerical models to simulate a buoyant plume rising beneath spreading plates and systematically test the effects of thermal, melt depletion, and melt retention buoyancy forces. Our second objective was to constrain the temperature anomaly, dimension, and volume flux of the Iceland plume by comparing theoretical predictions with observed variations in seismic crustal thickness, topography, gravity, and geochemistry on Iceland and along the Mid-Atlantic Ridge. We propose two end-member models for the mantle plume source beneath Iceland to explain the observations, and discuss their implications on basalt geochemistry, melt migration, and seismic velocity variations along the Mid-Atlantic Ridge axis.

2. Governing equations

To model mantle flow of a plume–ridge system in the upper mantle, we treat the mantle as a fluid of zero Reynolds number and infinite Prandtl number. The 3D stress tensor, τ, is defined according to:

$$\tau = 2\eta(T_R,p)\,\dot{\epsilon} - p\boldsymbol{I} \tag{1}$$

where $\boldsymbol{I}$ is the identity matrix and η is viscosity, which depends on real temperature T_R and hydrostatic pressure p. The strain rate tensor $\dot{\epsilon}$ depends on spatial derivatives of mantle flow rate $\boldsymbol{u}$ according to $\dot{\epsilon} = 1/2(\boldsymbol{u}_{i,j} + \boldsymbol{u}_{j,i})$. The equilibrium equations include conservation of mass:

$$\nabla \cdot \boldsymbol{u} = 0 \tag{2}$$

momentum:

$$\nabla \cdot \tau = -\Delta\rho(T,X,\phi)\,g\hat{z} \tag{3}$$

and energy:

$$\frac{\partial T}{\partial t} = \kappa\nabla^2 T - u \cdot \nabla T - \frac{T\Delta S}{c_p}\dot{M} \tag{4}$$

(see Table 1 for definition of variables). Eq. (2) satisfies the Boussinesq approximation and neglects dilational flow due to the extraction of melt, which is likely to be small [19]. Eq. (3) balances viscous stresses with the body force due to density varia-
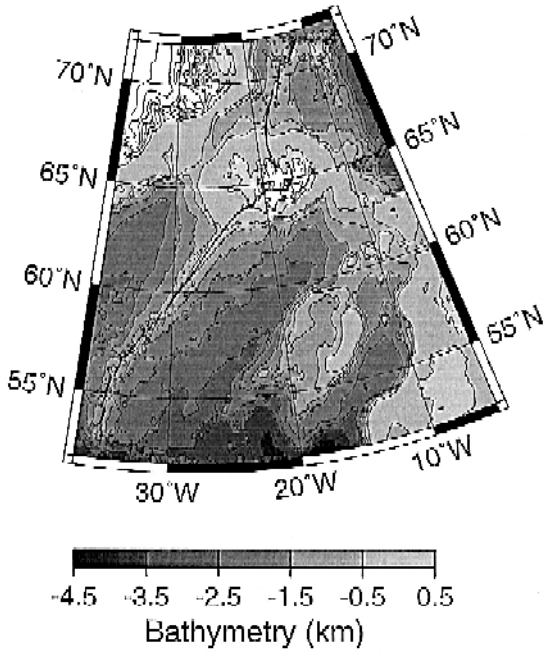
Fig. 1. Combined shipboard and Etopo5 bathymetry map (contour interval of 0.5 km) showing Iceland (65°N, 18°W) and the Reykjanes (south of Iceland) and Kolbeinsey (north of Iceland) ridges. Bold lines mark the ridge axes. This figure and Fig. 4, Fig. 7, Fig. 8 and Fig. 10, were produced using the GMT software package [48].

tions, which depend on potential temperature T, melt depletion X, and mantle porosity ϕ, according to:

$$\Delta\rho = -\rho_o\left(\alpha T + \beta X + \frac{\rho_o - \rho_m}{\rho_o}\phi\right) \tag{5}$$

Eq. (4) balances energy transfer associated with heat conduction, heat advection, and latent heat loss due to melting. Melt depletion is governed by:

$$\frac{\partial X}{\partial t} = -\mathbf{u}\cdot\nabla X + \dot{M} \tag{6}$$

where M is melt fraction and $\dot{M} = (\partial M(p,T))/(\partial t)$.

To estimate the distribution of porosity ϕ, we assume that melt migrates vertically through the mantle at a melt–mantle velocity contrast $(\omega - w)$ as governed by Darcy's flow law:

$$\phi(\omega - w) = \frac{(\rho_o - \rho_m)gK}{\eta_m} \tag{7}$$

Permeability K depends on grain size b according to $K = (b^2\phi^2)/(72\pi)$. Finally, the rate of melt percolation is assumed to be equivalent to the rate at which melt is generated such that:

$$\phi(z)\omega(z) = \frac{\rho_o}{\rho_m}\int_D^z \dot{M}\,\mathrm{d}z \tag{8}$$

3. Numerical method and boundary conditions

To solve the above equations, we use a Cartesian numerical code presented by Gable [20,21]. Time integration is achieved by iterating through discrete time steps, during each of which we solve for mantle flow, mantle potential temperature, and melt depletion. In solving the dimensionless forms of the flow equations (Eq. (1) Eq. (2) Eq. (3) Eq. (4)), horizontal derivatives are expressed in terms of their Fourier components while vertical derivatives are expressed as finite difference approximations. We then invert for horizontal and vertical components of velocities and stresses using a standard relaxation method.

The dimensionless form of Eq. (3) is:

$$\nabla\cdot\tau' = \frac{\rho_o gD^3}{\kappa\eta_o}\left(\alpha T_o T' + \beta X + \frac{\rho_o - \rho_m}{\rho_o}\phi\right) \tag{9}$$

where primes denote dimensionless variables. The body force (right hand side of Eq. (9)) is the sum of three terms: the first term, which scales with T', is a Rayleigh number:

$$Ra = \frac{\rho_o gD^3}{\kappa\eta_o}\alpha T_o$$

the second term, which scales with X, is a melt depletion Rayleigh number:

$$Ra_X = \frac{\rho_o gD^3}{\kappa\eta_o}\beta$$

and the third term, which scales with ϕ, is a melt retention Rayleigh number:

$$Ra_\phi = \frac{\rho_o gD^3}{\kappa\eta_o}\left(\frac{\rho_o - \rho_m}{\rho_o}\right)$$

Assumed values for β and $(\rho_o - \rho_m)/\rho_o$ are 0.06 [12,16] and 0.121 [14,18], respectively. Conse-

quently, depleting the mantle by 25% yields a density reduction equivalent to heating the mantle by 440°C, while a melt porosity of 3% yields a density reduction equivalent to heating the mantle by 107°C.

We assume that mantle viscosity varies with real temperature, T_R, and pressure according to:

$$\eta = \eta_o \exp\left\{ \frac{E + pV}{RT_R} - \frac{E + \rho_o\, g\,(0.5D)V}{RT_{Ro}} \right\} \quad (10)$$

where reference viscosity η_o is defined as the mantle viscosity for $T = T_o$ and $z = 0.5D$; T_R in Kelvin is $(T + 0.6z + 273)$, where the term $0.6z$ takes into account the adiabatic gradient; and T_{Ro} is the real temperature value of T_o. To approximate numerically the effects of non-Newtonian rheology, we use reduced values of activation energy E and activation volume V [22] (Table 1). Because lateral variations in viscosity introduce nonlinearity to the above flow

Table 1
Notation

Variable	Meaning	Value	Units
a	plume radius		km
b	grain size	3×10^{-4}	m
B	buoyancy number		
c_p	specific heat	1000	J kg^{-1}°C^{-1}
D	fluid depth	400	km
E	activation energy	1.9×10^5	J
g	acceleration of gravity	9.8	m/s
Δh_c	isostatic crustal topography		km
Δh_m	mantle dynamic topography		km
K	mantle permeability		m^2
M	melt fraction		wt%
p	pressure		Pa
P	plume tracer concentration		
Q	volumetric plume flux		km^3/my
R	gas constant	8.314	J K^{-1} mol^{-1}
Ra	thermal Rayleigh number		
Ra_X	depletion Rayleigh number		
Ra_ϕ	retention Rayleigh number		
ΔS	entropy change on melting	400	J kg^{-1}°C
T	mantle potential temperature		°C
T_R	mantle real temperature		K
ΔT_p	plume temperature anomaly		°C
$\mathbf{u}(u,v,w)$	mantle flow rate vector		km/my
U	ridge full spreading rate		km/my
V	activation volume	4×10^{-6}	m^3
W	along-axis plume width		km
X	melt depletion		wt%
α	coefficient of thermal expansion	3.4×10^{-5}	K^{-1}
β	coefficient of depletion density reduction		
γ	η_o/η_p		
κ	thermal diffusivity	31	km^2/my
η	viscosity		Pa s
η_o	reference viscosity		Pa s
η_p	plume viscosity at $0.5D$		Pa s
η_m	melt viscosity	1.0	Pa s
ω	vertical melt flow rate		km/my
ρ	mantle density		kg/m^3
ρ_c	crust density	2800–3030	kg/m^3
ρ_m	melt density	2900	kg/m^3
ρ_o	mantle reference density	3300	kg/m^3
ρ_w	water density	1000	kg/m^3

equations, we linearized the equations by introducing additional body force terms [20,23]. The nonlinear terms and solutions were then updated upon successive iterations until solutions converged to our specified limit. We found that a convergence criterion of 0.1–0.5% yielded time-integrated solutions with errors of < 0.5% while minimizing computing time. This computational method was tested in 2D with independent finite element solutions, while in 3D it produced solutions within 2.6% of the best-estimated extrapolated solutions of a benchmark problem of [24].

The final velocity field is then used in the advection term in Eq. (4) to solve for a new temperature field. Our energy solver uses finite differences with a tensor diffusion scheme to reduce numerical diffusion, which is intrinsic to finite difference methods [20,21]. The same tensor diffusion method is used to solve Eq. (6) for the depletion field. Vertical flow

determines the rate of decompression melting, comprising the source terms in Eq. (4) and Eq. (6). The melting rate term in Eq. (4) is latent heat loss, which inhibits buoyant mantle flow by increasing both mantle density and viscosity, while the melting rate term in Eq. (6) generates low density depleted mantle residuum. To calculate melting rate $\dot{M}$, we incorporate the solidus and liquidus functions of McKenzie and Bickle [25], as well as their functional dependence of M on homologous temperature for adiabatic batch melting.

The rate of melting also determines the volume fraction of melt retained in the mantle, ϕ, which is the source of retention buoyancy. To compute porosity we combine Eq. (7) and Eq. (8) and solve the integral in Eq. (8) numerically similar to [18]. The grain size dependent melt permeability that we incorporate results in maximum porosities of 1–3%, which is slightly higher than the 0.1–1% porosity range
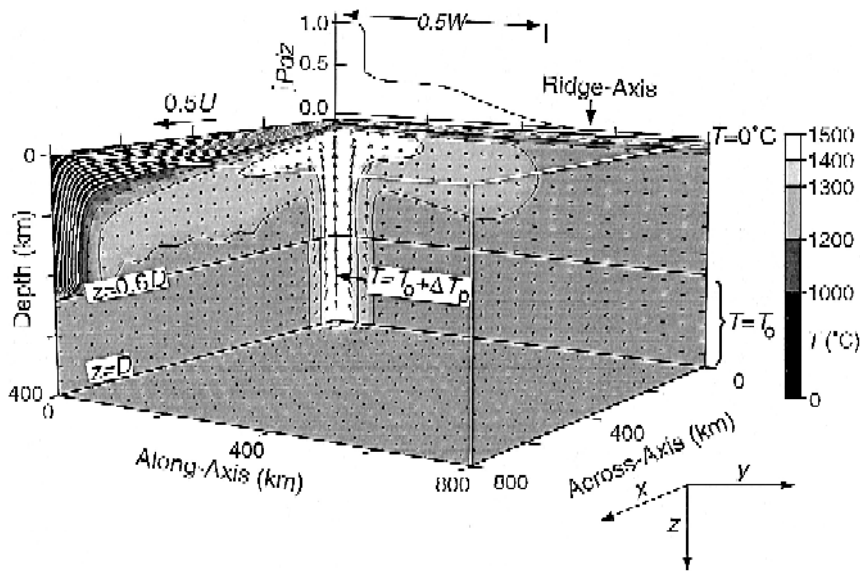

Fig. 2. Perspective diagram illustrating steady-state flow (small arrows) and potential temperature (shaded and contoured at 100°C intervals) fields of an example calculation that considers thermal buoyancy only and no melting effects (model 5a). Vertical plane on the right is a depth cross-section along the ridge axis ($x = 0$), while the vertical plane to the left is a depth cross-section perpendicular to the ridge axis ($y = 0$). Top plot shows depth-averaged plume tracer concentration, P, along the ridge axis, which we used to define plume width W. Both top ($z = 0$) and bottom ($z = D$) boundaries are isothermal planes with the bottom, a free slip boundary and the top, fixed at a horizontal velocity of $0.5U$ (large horizontal arrow). All boundaries are closed to flow both in and out of the numerical box, thus material flows downward at the end of the box opposite the ridge ($x = 800$ km) and recirculates toward the ridge axis along the base of the box. The effect of this recirculation on the interaction between plume and ridge are insignificant.

Table 2
Parameters and results of experimental sets

Model	Grid size $dx - dy$ (km)	U (km/my)	ΔT_p	B	γ	Q (10^6 km^3/my)	W	$W(Q/U)^{-1/2}$
Set A: thermal buoyancy without latent heat loss								
1a	12.5–12.5	20	100	1.729	2.352	0.974	512	2.322
2a	12.5–6.25	120	100	0.0522	2.352	1.059	219	2.328
3a	12.5–6.25	60	100	0.195	2.352	0.987	281	2.193
4a	12.5–6.25	40	100	0.460	2.352	1.038	362	2.251
5a	12.5–12.5	20	200	6.977	5.054	1.965	938	2.991
6a	12.5–6.25	120	200	0.244	5.054	2.478	331	2.305
7a	12.5–6.25	60	200	0.746	5.054	1.892	419	2.358
8a	12.5–12.5	50	200	1.468	5.054	2.585	662	2.914
Ice 1a	12.5–12.5	19	75	36.553	1.849	12.39	2312	2.864
Ice 2a	10.0–10.0	19	170	14.866	3.757	2.186	830	2.447
Set B: thermal buoyancy with latent heat loss								
1b	12.5–12.5	20	100	1.720	2.352	0.969	488	2.215
2b	12.5–6.25	120	100	0.0463	2.352	0.939	206	2.331
3b	12.5–6.25	60	100	0.166	2.352	0.843	256	2.162
4b	12.5–6.25	40	100	0.389	2.352	0.876	312	2.111
5b	12.5–12.5	20	200	7.001	5.054	1.972	838	2.667
6b	12.5–6.25	120	200	0.203	5.054	2.059	281	2.147
7b	12.5–6.25	60	200	0.750	5.054	1.901	369	2.072
8b	12.5–12.5	50	200	1.193	5.054	2.100	462	2.257
Ice 1b	12.5–12.5	19	75	34.774	1.849	11.79	2212	2.809
Ice 2b	10.0–10.0	19	170	14.857	3.757	2.185	710	2.094

Set C: thermal + depletion buoyancy with latent heat loss

1c	12.5–12.5	20	100	1.427	2.352	0.804	488	2.431
2c	12.5–6.25	120	100	0.0452	2.352	0.917	206	2.360
3c	12.5–6.25	60	100	0.164	2.352	0.834	256	2.173
4c	12.5–12.5	40	100	0.385	2.352	0.868	338	2.291
5c	12.5–12.5	20	200	6.788	5.054	1.912	988	3.194
6c	12.5–6.25	120	200	0.188	5.054	1.902	281	2.234
7c	12.5–6.25	60	200	0.724	5.054	1.835	406	2.323
8c	12.5–12.5	50	200	1.159	5.054	2.040	538	2.661
Ice 1c	12.5–12.5	19	75	34.117	1.849	11.56	2288	2.932
Ice 2c	10.0–10.0	19	170	14.597	3.757	2.147	830	2.469

Set D: thermal + depletion + retention buoyancy with latent heat loss

1d	12.5–12.5	20	100	1.433	2.352	0.808	488	2.426
2d	12.5–6.25	120	100	0.0452	2.352	0.917	206	2.359
3d	12.5–6.25	60	100	0.1648	2.352	0.836	256	2.171
4d	12.5–12.5	40	100	0.358	2.352	0.868	338	2.292
5d	12.5–12.5	20	200	6.764	5.054	1.905	913	2.956
6d	12.5–6.25	120	200	0.193	5.054	1.961	281	2.200
7d	12.5–6.25	60	200	0.718	5.054	1.820	419	2.404
8d	12.5–12.5	50	200	1.139	5.054	2.005	563	2.809
Ice 1d	12.5–12.5	19	75	34.089	1.849	11.56	2288	2.933
Ice 2d	10.0–10.0	19	170	14.501	3.757	2.133	870	2.597

For all experiments vertical grid separation dz is 8 km. Models 1–8: $\beta = 0.06$, $\Delta T = 1300°C$, $\eta_o = 1 \times 10^{20}$ Pa s, $Ra = 0.915 \times 10^6$, $Ra_X = 1.35 \times 10^6$, $Ra_\phi = 2.75 \times 10^6$, $\alpha = 70$ km. Models Ice 1 and 2: $\beta = 0.024$, $\Delta T = 1350°C$, $\eta_o = 5 \times 10^{19}$ Pa s, $Ra = 1.90 \times 10^6$, $Ra_X = 1.12 \times 10^6$, $Ra_\phi = 5.70 \times 10^6$. Model Ice 1: $a = 300$ km, $\Delta T_p = 75°C$. Model Ice 2: $a = 60$ km, $\Delta T_p = 170°C$.

inferred from ^{238}U–^{230}Th–^{226}Ra disequilibria in Hawaiian lavas [26].

The numerical model set-up is illustrated in Fig. 2. A ridge axis ($x = 0$) is simulated by defining reflecting temperature (i.e., zero heat flux) and flow (i.e., zero shear stress) boundary conditions at the vertical sides, and setting the top boundary ($z = 0$) to move at a constant half-spreading rate $0.5U$. Temperature at the surface ($z = 0$) is maintained at 0°C, which cools and thickens a high viscosity lithosphere approximately with the square-root of x. A plume is introduced by imposing a columnar-shaped temperature anomaly in the lower portion of the box, centered beneath the ridge axis. The plume is hottest ($T = T_o + \Delta T_p$) at its center and cools as a Gaussian function of radial distance to T_o at its radius a. We exploit the symmetry in x and y by centering the plume column at $x = y = 0$, which allows a quarter plume in solution space to represent a fully circular plume in virtual space. In the lower portion of the box ($z > 0.6D$), we impose the potential temperature to be T_o everywhere except inside the plume source. Thus, the energy equation is solved only in the upper portion of the box ($0.6D \geq z \geq 0$).

To ensure numerical accuracy in the flow solutions, we set a non-dimensional viscosity (η / η_o) upper limit of 200 and set a lower limit of 0.1. The upper viscosity limit is sufficient to simulate accurately a rigid lithosphere (i.e., $u = U$ and $v = w = 0$ in the lithosphere), while the lower limit allows us to incorporate the full viscosity reduction in a plume with temperature anomaly of 200°C. The depth dependence of viscosity yields a factor of ~ 4 viscosity increase between top and bottom of the box for a constant mantle temperature.

4. Steady-state along-axis width of a mantle plume head

We seek here to quantify the effects of melting on mantle flow and thus the dependence of along-axis plume width, W, on plume flux, Q, and plate spreading rate, U. We began numerical experiments with the steady-state temperature solution of a ridge without the plume. Then, after activating the plume, we integrated through time until both along-axis plume

width and plume flux converged to steady-state values. We ran four sets of experiments (Table 2): experimental set A includes only thermal buoyancy and omits all melting effects; set B considers only thermal buoyancy but includes latent heat loss; set C includes additional buoyancy from melt depletion; and set D includes additional buoyancy from melt retention.

Fig. 2 shows an example of steady-state velocity and temperature field for a calculation in set A with a plume source temperature anomaly of 200°C (model 5a). Velocity vectors illustrate the plume rising from the conduit source and then spreading both perpendicular to and along the ridge axis after it impinges on the base of the lithosphere. The combined effects of thermal buoyancy and reduced plume viscosity result in a maximum plume upwelling rate of 244 km/my, which is > 20 times that of the half spreading rate of 10 km/my. The corresponding average upwelling rate in the melting zone ($z \leq 110$ km) is 85 km/my.

Fig. 3a shows the steady-state velocity and mantle density fields for the same plume source temperature anomaly but with the additional effects of latent heat loss (model 5b). In the melting region of the plume center, potential temperatures are ~ 130°C cooler and consequently the plume is 65% less buoyant and 3 times more viscous than the calculation without latent heat loss (Fig. 2). The resulting average upwelling rate in the melting zone is 50 km/my, only $\sim 60\%$ of the predicted average upwelling rate of the model without latent heat loss (model 5a).

The addition of melt depletion buoyancy in model 5c generates an additional $\sim 1\%$ lateral density contrast between the plume center and the mantle beneath normal ridge sections far from the plume (Fig. 3b). The resulting average melting zone upwelling rate is 67 km/my. As material rises more rapidly in the plume center, it spreads more rapidly along the base of the rigid lithosphere. This in turn inhibits upwelling at radial distances of 100–150 km, shown as negative velocity differences in Fig. 3b.

Finally, model 5d considers the additional buoyancy from melt retention (Fig. 3c). The high melting rate in the plume center results in a maximum porosity of 2.5%, to reduce bulk density in the plume center by an additional 0.3%. This added retention buoyancy further enhances the average upwelling

rate in the melting zone to 77 km/my, which is ~ 90% of that predicted by the model that neglects all melting effects (model 5a). Thus, the added melting-related buoyancy forces approximately balance

the upwelling-inhibiting effects of latent heat loss.

In all models examined we find, as did Ribe et al. [11], that the thickening lithosphere does not channel the plume preferentially along the ridge axis. On the
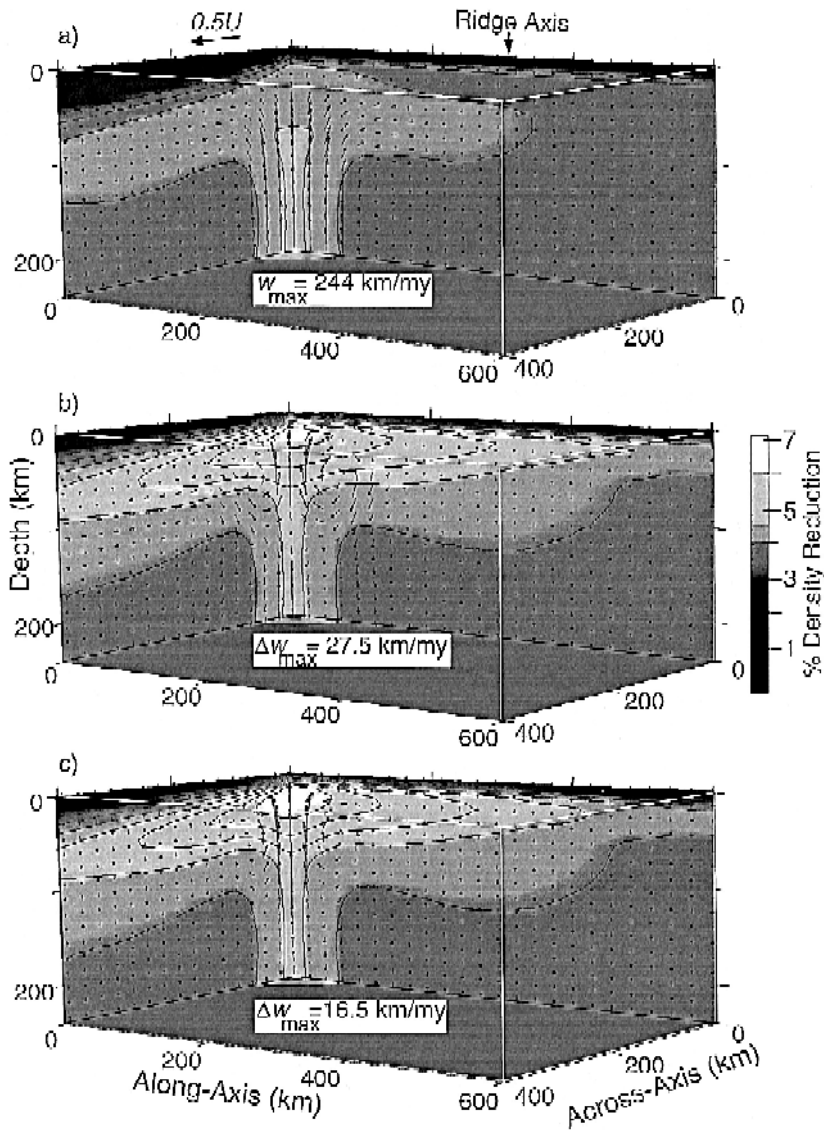

Fig. 3. Perspective views of depth cross-sections showing percentage density reduction in the mantle due to: (a) thermal buoyancy with latent heat loss ($\Delta T_p = 200°C$) (model 5b); (b) plus melt depletion buoyancy (model 5c); and (c) plus melt retention buoyancy (model 5d). Contour interval is 0.5%. Vectors in (a) show mantle flow. Vectors in (b) show the differences between flows with and without melt depletion buoyancy. Vectors in (c) show the difference between flows with and without melt retention buoyancy. Downward pointing vectors in (b) and (c) illustrate reduced upwelling, not downwelling.

contrary, the spreading lithosphere enhances ridge-perpendicular flow by pulling plume material away from the ridge-axis, and actually impedes along-axis flow by viscous shear. These effects however are small — the total along-axis flux at $y = 70$ km is within a few percent of the total ridge-perpendicular flux at $x = 70$ km. Thus, the rate of spreading away from the plume center is approximately equal in all radial directions.

To determine how W depends on Q and U for each experimental set, we examine spreading rates between 20 and 120 km/my and we vary Q by changing ΔT_p between 100°C and 200°C (Table 2). We track the distribution of plume material by introducing a tracer, P, in the plume and using our tensor diffusion scheme to advect P passively with the mantle. $P = 1$ is introduced in the plume source column to represent 100% plume material, while $P = 0$ represents 0% plume material and 100% ambient mantle. We define W as the along-axis extent to which the depth-integrated tracer concentration:

$$\left(\frac{1}{0.6D} \int_0^{0.6D} P(0, y, z) \, \mathrm{d}z \right)$$

is > 0.05 (Fig. 2). The volume flux of the plume is measured at $z = 0.6D$ by integrating the vertical flow of the plume source over its cross-sectional area.

For calculations that include thermal buoyancy only without latent heat loss (set A), we find, similar to [9,11], that W depends primarily on the scaling quantity $(Q/U)^{1/2}$, and depends secondarily on the plume buoyancy number ($B = (Q \rho_o \alpha \Delta T_p)/(48 \eta_o U^2)$), as defined in [11], and on the ambient/plume viscosity ratio $\gamma = \eta_o / \eta_p$, at $z = 0.5D$. A modified buoyancy number which depends on plume viscosity is thus ($B\gamma$). The best-fit linear regression function obtained by fitting linear and constant coefficients to $\ln(B\gamma)$ is:

$$W = 2.35 \left(\frac{Q}{U} \right)^{1/2} (B\gamma)^{0.04} \tag{11}$$

Calculated values of $W(Q/U)^{-1/2}$ range from 2.2 to 2.9 (Table 2) with a mean value of 2.50. To compare our results directly with those of Ribe et al. [11], we omit the dependence on γ and incorporate their definition of Q, which is the integrated vertical

plume flux weighted by plume temperature anomaly. With these modifications we obtain a best-fit linear regression of $W = 2.80(Q/U)^{1/2} B^{0.05}$ which is in good agreement with that of Ribe et al. [11] of $W = 2.93(Q/U)^{1/2} B^{0.052}$. While the scaling and exponential factors vary slightly between our results and those of [9] and [11], the general form of Eq. (11) is robust and insensitive to differences in far-field experimental boundary conditions.

For calculations of thermal buoyancy with latent heat loss (set B), we obtain a best-fit linear regression function:

$$W = 2.21 \left(\frac{Q}{U} \right)^{1/2} (B\gamma)^{0.02} \tag{12}$$

The smaller constant and exponential coefficients relative to those in Eq. (11) reflect the inhibiting effects of latent heat on along-axis plume spreading. The average values of $W(Q/U)^{-1/2}$ for experimental set B is 2.29, or $\sim 92\%$ of the average in set A.

Addition of depletion buoyancy in experimental set C results in a best-fit regression function:

$$W = 2.37 \left(\frac{Q}{U} \right)^{1/2} (B\gamma)^{0.04} \tag{13}$$

This function is essentially the same as that of Eq. (11) for set A. The average value of $W(Q/U)^{-1/2}$
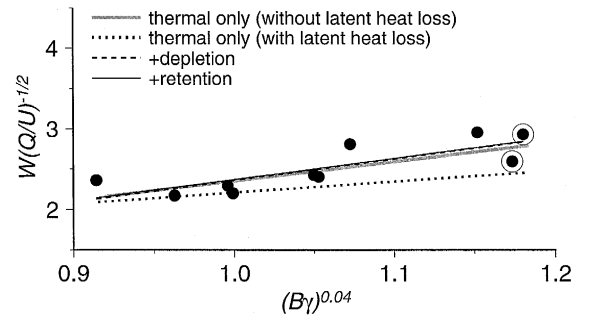

Fig. 4. Numerical results (dots) of calculations with all melting effects included (set D). The two Iceland models are circled. The solid black line is the best-fit linear regression shown by Eq. (13), which yields a standard deviation misfit that is 7% of the median value of $W(Q/U)^{-1/2}$. Also shown are corresponding linear regressions of calculations of thermal buoyancy without latent heat loss (set A, gray), thermal buoyancy with latent heat loss (set B, dotted), and additional buoyancy from melt depletion (set C, dashed).

of 2.51 is also essentially the same as that in set A. The further addition of melt retention (set D) does not change this relationship significantly, as shown by the similarity in regression lines of set C and set D (Fig. 4). Thus, the effects of retention buoyancy occur at wavelengths too short to affect the full width W. In summary, the effects of latent heat loss to inhibit lateral plume spreading are approximately balanced by the added buoyancy of melt depletion which enhances plume spreading.

5. Models of Iceland and the Mid-Atlantic Ridge

We next investigate models of mantle flow and melting beneath Iceland, a relatively well studied example of a ridge-centered plume. Our objective is to constrain the temperature anomaly, dimension, and volume flux of the Iceland plume by comparing theoretical model predictions with observed along-axis variations in seismic crustal thickness, topography, gravity, and basalt geochemistry. Previous geophysical studies of the Iceland–MAR system demonstrated that the topographic high at Iceland coincides with a low in mantle Bouguer gravity anomaly (MBA), and that both MBA and topographic anomalies can be explained by the combined effects of anomalously thick crust and low density mantle generated by the Iceland plume [27,28]. MBA are calculated by subtracting from free-air gravity the attraction of seafloor topography and the crust–mantle interface, assuming a uniform crustal thickness of 7 km (e.g., [29,30]). Because as much as 75% of the along-axis topographic and MBA variations may arise from thickened igneous crust [28,31], crustal thickness calculations are an important link between our models and surface observations.

To predict crustal thickness from mantle melting calculations, we assume that all melt generated within 200 km of the ridge-axis accretes perpendicularly to the ridge-axis and take the top of our numerical box to be the isostatic depth of the seafloor for crust of normal thickness (7 km). The crustal thickness as a function of along-axis coordinate y is therefore:

$$Cr(y) = \frac{2}{U}\left(\frac{\rho_o}{\rho_m}\right)\int \dot{M}(y)\,\mathrm{d}x\,\mathrm{d}z \qquad (14)$$

We take the top of our model to be the isostatic depth of the seafloor for a 7 km thick model crust, and assume isostatic compensation of crustal thickness variations that deviate from this model crust. Consequently, variations in crustal thickness impart no lithostatic pressure variations in the mantle. To prevent melting at depths shallower than the isostatic base of the thickened Icelandic crust we prohibit melting everywhere at depths < 28 km. Melting may stop deeper, however, if hydrothermal cooling is important [32].

To calculate isostatic topography of the seafloor, we consider contributions from both the crust (Δh_c) and mantle (Δh_m). In calculating Δh_c, we assume Airy compensation of the crust with a surface density contrast of ($\rho_c - \rho_w$) for the submarine portion of topography and ρ_c for the subaerial portion. The crust along the Reykjanes and Kolbeinsey ridges is assumed to have a density of 2800 kg/m^3, except within 500 km of the plume center, where we increase it linearly to a maximum of 3030 kg/m^3 at Iceland, to account for the higher MgO content of the Icelandic crust [33]. The mantle contribution to topography, or dynamic topography is calculated from vertical normal stress at the top layer of our model:

$$\Delta h_m = \frac{\tau_{zz}}{(\rho_o - \rho_w)g} \qquad (15)$$

With this definition, our calculations predict seafloor depths to increase approximately with the square-root of distance from the ridge-axis, which is consistent with lithospheric half space cooling models (e.g. [34]). In addition to using Δh_m to predict topography, we also use Δh_m to estimate crustal thickness in a manner independent of our mantle melting calculations. This 'isostatic crustal thickness' is defined as the isostatic thickness of crust required to account for the difference between the observed topography and Δh_m.

In computing MBA we again consider both crustal and mantle contributions. The crustal contribution is the gravitational signal due to undulations at the crust–mantle interface that deviate from the constant crustal thickness reference model originally assumed in generating MBA. For these calculations we employ the method of [35]. The mantle contribution to

gravity is calculated by integrating the contributions from lateral density variations at each model layer [29].

5.1. Broad plume source model

Our first model of the Iceland–MAR system, much like that of Ribe et al. [11], considers a broad plume source with a relatively small temperature anomaly (model Ice 1, $a = 300$ km, and $\Delta T_p = 75°C$) rising beneath a model MAR with a full spreading rate of 19 km/my [36] (Fig. 5a). At this spreading rate, $T_o = 1350°C$ is required to produce a ~ 7 km thick, normal oceanic crust. The calculation that includes all melting effects (model Ice 1d) predicts a plume volume flux of $\sim 1.2 \times 10^7$ km³/my, generating an along-axis plume-head width, W, of ~ 2300 km (Fig. 5a). The predicted maximum upwelling rate in model Ice 1d is 105 km/my, which is > 10 times that beneath the unaffected portion of the ridge far from the plume. The predicted upwelling rate averaged through the melting zone in the plume center is 20 km/my. Melt retention buoyancy contributes minimal effects to this average upwelling rate and thus very little to melting rate.

The enhanced upwelling rate in the plume center, combined with an increase in total melt extent (23% compared to 13% beneath the ridge far away from the plume), generates a maximum crustal thickness of ~ 30 km, consistent with the seismic measurements on Iceland [37] (Fig. 5b). Along the length of the Reykjanes Ridge, the crustal thickness profiles predicted by melting in model Ice 1d shows striking similarity to the seismic measurements. From the plume center, the predicted crust first thins to 9.5 km at an along-axis distance of ~ 300 km, then thickens to 11 km at a distance of ~ 500 km, and finally tapers to a thickness of 6.7 km at a distance of ~ 1300 km. The predicted local minimum in crustal thickness at $y \sim 300$ km is caused by a reduced mantle upwelling rate at the plume edge, caused by the rapid vertical flux in the plume center. Melt retention does not significantly affect crustal thickness because the predicted 0.5% contrast in porosity between the plume center and normal sub-ridge mantle is too small to appreciably enhance plume upwelling rate in the shallowest 100 km, where melting occurs. The isostatic crustal thickness profile of model Ice 1d also shows good agreement with the observed crustal thickness profile (Fig. 5b). The excess magmatic flux rate required to sustain the anomalous (in excess of a 7 km thick) isostatic crust along the MAR, 1000 km north and south of Iceland, is 2.33×10^5 km³/my. This value is within a few percent of the 2.45×10^5 km³/my excess crustal production rate predicted from our melting model.

The predicted topography from the melting-model crustal profile generates 70% (~ 2.5 km) of the total along-axis topographic anomaly of ~ 3.5 km (Fig. 5c). We predict the remaining 30% (~ 1 km) of topography to be supported by dynamic mantle uplift which is obtained with a β value of 0.024 [12,17]. Of mantle dynamic topography, Δh_m, thermal buoyancy generates $\sim 70\%$ while depletion and retention buoyancy generate the remaining 22% and 8%, respectively. The predicted total amplitude of Δh_m is consistent with the 0.5–1.5 km of Eocene uplift as inferred from sediment core analyses [38].

The mantle Bouguer anomaly along the submarine portions of the ridge is also matched well by predictions of model Ice 1d using both the melting model and isostatic crust (Fig. 5d). Similar to bathymetry, the crustal MBA accounts for most (70%) of the total predicted anomaly of ~ 330 mGal, with the mantle contributing the remaining 30%. Of the predicted mantle gravity signal, 75% is from thermal expansion, while 20% and 5% are generated by melt depletion and retention, respectively. The successful predictions of both topography and MBA support the hypothesis that these anomalies are from the same sources: primarily crustal thickness variations and secondarily density variations in the shallow mantle.

5.2. Narrow plume source model

Our second set of models (Ice 2) represent another end-member possibility — that of a narrower and hotter plume source (Fig. 6a; $a = 60$ km, and $\Delta T_p = 170°C$). With all melting effects included, model Ice 2d predicts a plume volume flux of 2.1×10^6 km³/my, which spreads plume material to a full width, W, of 870 km along the ridge axis. The maximum upwelling rate of model Ice 2d is 283 km/my, which is > 2.5 times greater than the maximum upwelling rate in the broad plume source (model
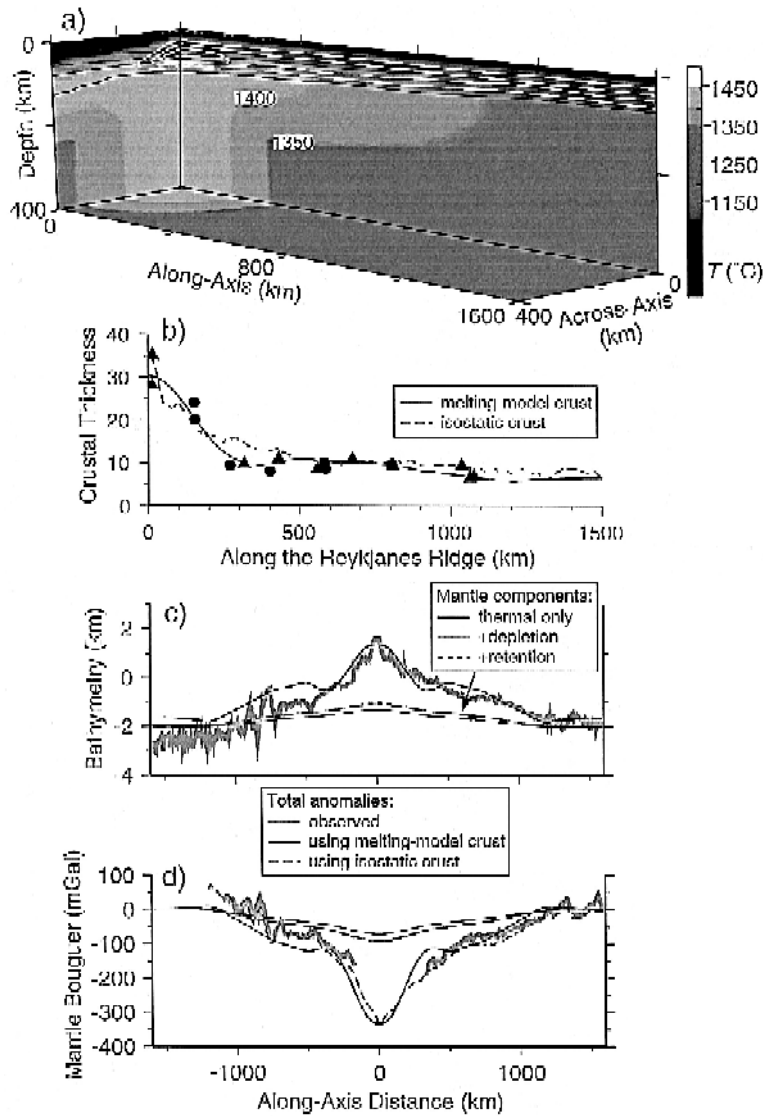
Fig. 5. (a) Perspective diagram of model Ice 1d (broad plume source) shaded according to temperature. Black contours are depletion (contour interval is 5%) and white contours are melting rates of 0.01, 0.03, and 0.05 my^{-1}. (b) Comparison between model Ice 1d melting model crust (solid) and isostatic crust (dashed), and seismic crustal thickness measurements along the Reykjanes Ridge (dots) and at older seafloor near the continental margins (triangles) from [37]. (c) and (d) Comparison between the observed bathymetry (thick gray curve in c) and MBA (thick gray curve in d) along the MAR and predicted profiles of model Ice 1d using the melting model crust (bold curves in c and d) and isostatic crust (thick dashed curved in d). Also shown are predicted mantle components due to various mantle density sources as labeled. Bathymetry data and MBA are from [28]. We do not consider the on-land gravity of Iceland.

Ice 1d), and ∼ 30 time faster than normal ridge upwelling rates. In addition, the maximum extent of melting is increased to 30%. Thus, a larger volume of mantle material is predicted to circulate more rapidly through a thicker melting zone relative to that of Ice 1d, which results in melting rates an order of magnitude greater than those in model Ice 1d (Fig. 6a). For the model without melt retention (model Ice 2c), the melting-zone averaged upwelling rate is 63 km/my and the maximum melting model crustal
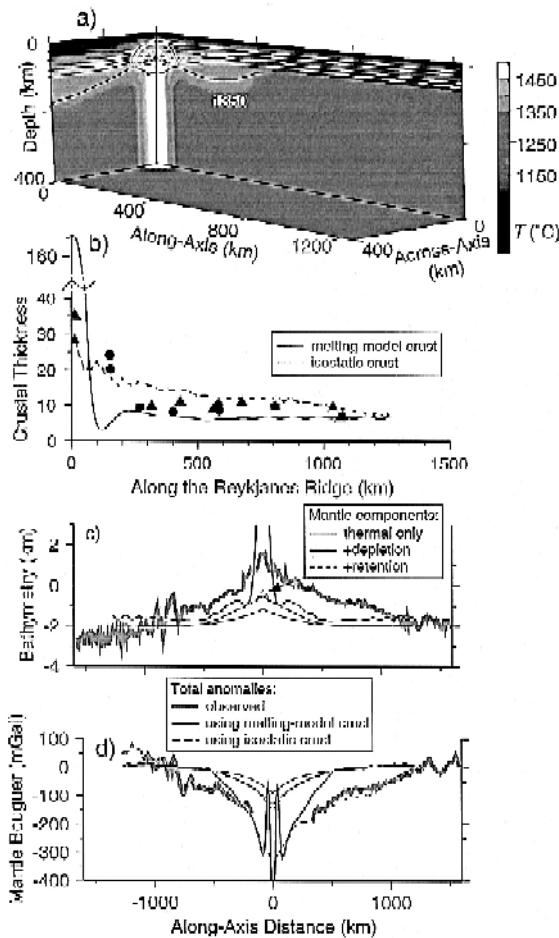
Fig. 6. As Fig. 5 but for Ice 2 models (narrow plume source). Symbols as in Fig. 5 except melting rate contours in (a) are 0.01, 0.03, 0.05, 0.2 and 0.4 my^{-1}.

thickness is 147 km. With melt retention (model Ice 2d), the 2.9% porosity in the plume is sufficient to increase the predicted melting-zone-averaged upwelling rate to 80 km/my and the maximum melting-model crustal thickness to 166 km (Fig. 6b). In model Ice 2d, the melting-model crust thins to 3 km at an along-axis distance of 120 km, where upwelling and thus melting rate is strongly reduced at the edge of the rapidly upwelling plume center (Fig. 6a).

The high maximum crustal thicknesses predicted by the narrow plume source melting model drastically exceed calculations of previous studies that assumed passive mantle upwelling (e.g. [28,39]) and

drastically exceed the observed crustal thicknesses (Fig. 6b). The resulting topographic and MBA anomalies also fail to match the observations (Fig. 6c,d). The isostatic crustal profile, on the other hand, yields predictions in much better agreement with the observed crustal thicknesses (Fig. 6b), topography (by definition) (Fig. 6c), and MBA (Fig. 6d) along the ridge-axis. Thus, if the Iceland plume is comparable in radius and temperature to our narrow plume source model, a substantial portion of the melt produced beneath Iceland must accrete more uniformly along-axis than our melting-model crust, much like our isostatic crustal profile. This condition suggests melt migration and/or lower crustal ductile flow [40] occurs over distances of several hundreds of kilometers away from Iceland, along the Reykjanes and Kolbeinsey ridges.

Because the mechanisms of along-ridge-axis melt transport are poorly understood, we do not attempt to model this process in this study. Instead, we assume a priori that along-axis melt redistribution does occur and that the end result of this process leads to the isostatic crustal profile. In arriving at our final Ice 2 models, we thus sought values of ΔT_p and a such that the total volume rate of melt produced by the melting model matched that required to sustain the isostatic crustal profile. The best solutions of $\Delta T_p = 170°C$ and $a = 60$ km yield a total excess melt production rate of 2.54×10^5 km^3/my (model Ice 2d), which is within 1% of that required of the isostatic crustal profile.

In these narrower, hotter plume source models, the mantle contribution to topography and gravity relative to the crustal contribution becomes much larger than in the broader, cooler source models. For example, model Ice 2d predicts a mantle topographic uplift that is 51% (1.8 km) of the observed along-axis topographic anomaly (Fig. 6c), and a mantle contribution to MBA that is 48% (158 mGal) of the observed MBA variation (Fig. 6d). The crust therefore generates only 49% and 52% of the total topographic and MBA variations, respectively. Calculations also predict the importance of melt-related buoyancy to the mantle anomalies to be significantly greater for these hotter plume source models relative to the cooler source models. Thermal buoyancy is predicted to produce 47% of Δh_m, and 60% of the mantle MBA variation; melt depletion produces 39%

of Δh_m and 25% of the mantle MBA; and melt retention produces the remaining 14% of Δh_m and 15% of the mantle MBA variation.

5.3. Reykjanes Ridge bathymetric swell

Similar to along-axis topography, we predict map view topography by adding mantle dynamic topography (Eq. (15)) and isostatic topography of the crust considering only along-axis variations in crustal thickness. For model Ice 1d, we use the melting-model crust and for model Ice 2d, we use the isostatic crust. Fig. 7 illustrates the observed topography in map view along the Reykjanes Ridge south of Iceland, and predictions of models Ice 1d and Ice 2d. The similarity between the predictions and observations at broad wavelengths ($> \sim 500$ km) are compelling: both models predict the ~ 2.0 km across-axis decrease in broad wavelength topography between Iceland and an across-axis distance of 400 km away from the ridge-axis, and both predict the south-pointing swell, elongated along the Reykjanes Ridge. As demonstrated above, the southward deepening of the ridge axis reflects crustal thinning and mantle density increase with distance from the Iceland plume source. But perpendicular to the ridge-axis, seafloor topography is dominated by the subsidence of the cooling lithosphere. Thus, contrary to previous notions (e.g. [5,6]), the regional bathymetric swell does not require a pipe-like flow of plume material along the ridge axis. Instead, we predict the plume head to spread radially and explain the general shape of the elongated Icelandic swell as the superposition of radial plume spreading and across-axis lithospheric cooling. The models presented in this study, however, do not consider time-dependent variations in crustal accretion which may also contribute to across-axis topographic variations.
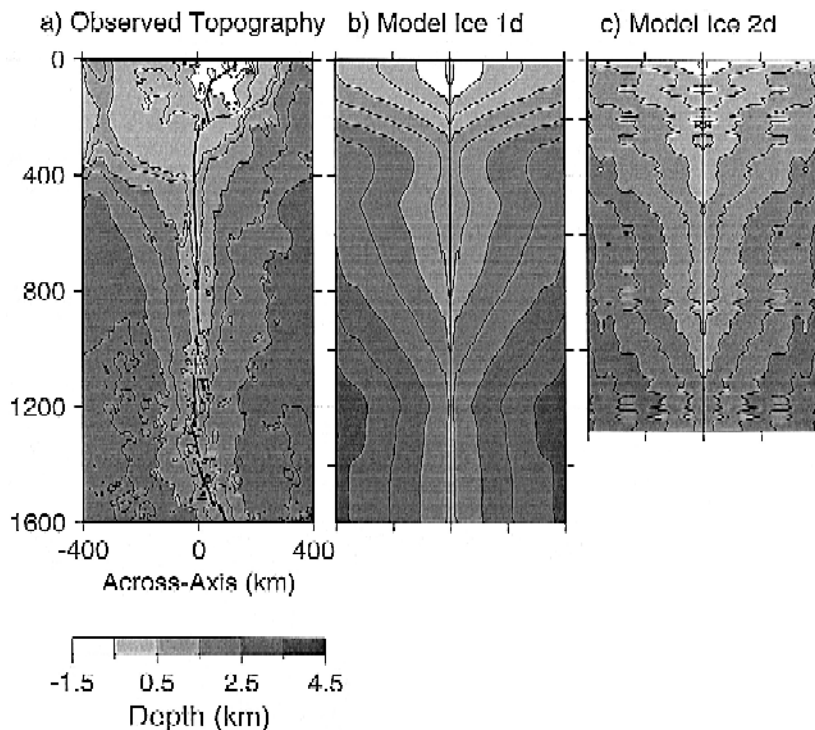

Fig. 7. (a) Observed topography of Iceland and the Reykjanes Ridge (oblique Mercator projection). (b) Mantle + crustal topography predicted from our broad plume source model Ice 1d using the melting model crust. (c) Mantle + crustal topography predicted from our narrow plume source model Ice 2d using the isostatic crust.

5.4. Rare earth element and isotopic anomalies

A potentially useful independent constraint on melting depth and extents, which reflect mantle temperature, is rare earth element (REE) concentrations of axial basalts. A simple comparison can be made
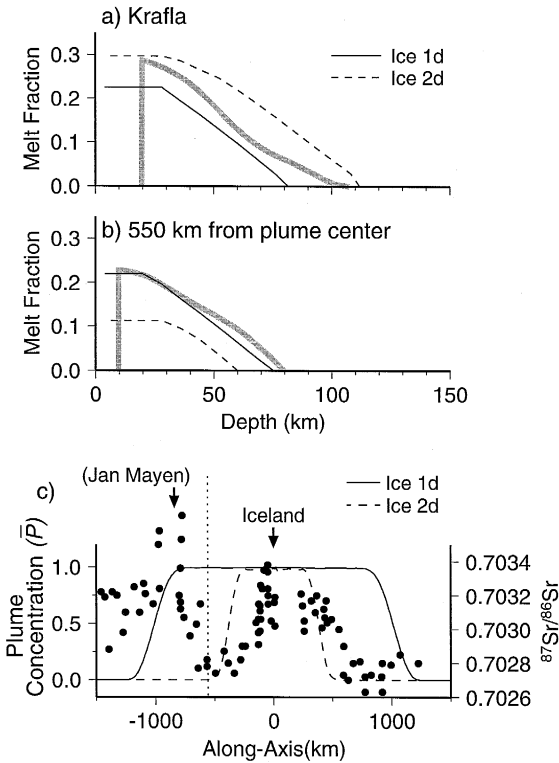

Fig. 8. (a) and (b) Comparison between White et al.'s [33] REE inversion of melt fraction (gray) and our predictions from models Ice 1d (solid) and Ice 2d (dashed) at Krafla, near the plume center (a), and at DSDP Site 409 on the Reykjanes Ridge 550 km away from the plume center (b). This inversion method assumes fractional melting and includes differences in partitioning coefficients between the spinel and garnet stability fields. It also assumes complete extraction and mixing of all melts generated in the melting region, which makes the estimation of maximum depth of melting sensitive to the low-degree melt compositions [49]. Another assumption is the parent source composition (primitive mantle beneath Krafla and a 50–50% mix of primitive and depleted MORB source along the Reykjanes Ridge), which is important in estimating the maximum extent of melting. (c) Comparison between observed Sr isotope concentrations [41] along Iceland and the MAR and weighted mean plume tracer concentration $\overline{P}$ in the accumulated melts for models Ice 1d (solid) and Ice 2d (dashed). The peak in $^{87}Sr/^{86}Sr$ to the north of Iceland is due to the Jan Mayen hotspot [41] which we do not model.

with previous inversions of melt fraction versus depth as calculated by White et al. [33]. At the plume center, our broad plume source model (Ice 1d) and narrow plume source model (Ice 2d) predict melt fractions that are lower and higher, respectively, than White et al.'s [33] inversions for Krafla volcano on Iceland (Fig. 8a). The potential temperature of the Iceland plume source, therefore, is likely to be 1425–1520°C, as represented by our two end-member models. At ～550 km from Iceland on the Reykjanes Ridge, model Ice 1d predicts melting depths and extents closely matching those obtained from the REE inversions [33] (Fig. 8b). Model Ice 2d, however, underpredicts the extents and depths because plume material from our narrow plume source did not spread to this along-axis distance. Thus, in order to explain the REE composition of basalts sampled 550 km away from Iceland, once again our model Ice 2d seems to require plume-derived melts to migrate substantially along the Reykjanes Ridge axis.

While REE concentrations reflect melting process beneath Iceland, Sr isotope ratios may reflect the concentration of the plume source material relative to that of normal mid-ocean ridge basalts (MORB). Schilling [8,41] interprets the peak in $^{87}Sr/^{86}Sr$ at Iceland to mark the center of the Iceland plume, where the plume source concentration is highest, and interprets the decrease in $^{87}Sr/^{86}Sr$ north and south of Iceland to reflect a decrease in percent of plume material comprising the mantle melt source.

To address questions of where and how plume–MORB mixing occurs, we calculate the fraction of plume tracer, P, in accumulated melts along the model ridge-axis (neglecting along-axis melt migration) (Fig. 8c). At each numerical grid where new melt is generated, P is weighted by melting rate. We then integrated over each ridge-perpendicular plane to compute a weighted mean value ($\overline{P}$) for each point along the ridge axis:

$$\overline{P}(y) = \frac{\int P(x,y,z)\dot{M}(x,y,z)\mathrm{d}x\mathrm{d}z}{\int \dot{M}(x,y,z)\mathrm{d}x\mathrm{d}z} \qquad (16)$$

This calculation thus approximates the plume concentration of pooled melts along the ridge axis. For example, $\overline{P} = 1.0$ indicates that all of the melt generated in a plane perpendicular to that point of the

ridge is entirely plume source derived. Likewise, $\bar{P} = 0.0$ indicates that none of the melts are plume derived and $0.0 < \bar{P} < 1.0$ indicates plume–MORB mixing.

Model Ice 1d predicts an along-axis geochemical plume width of > 2000 km, significantly greater than that suggested by the $^{87}Sr/^{86}Sr$ anomaly. Ice 2d, on the other hand, predicts a width of ~ 1000 km, which is more consistent with that of the $^{87}Sr/^{86}Sr$ anomaly; however, its profile in $\bar{P}$ would likely be broader if along-axis melt migration were considered. Both model Ice 1d and Ice 2d predict that the melts are entirely plume derived ($\bar{P} = 1.0$) over most of the plume width, and become fully ambient mantle derived ($\bar{P} = 0.0$) within 200–300 km of the edge of the plume. These results suggest
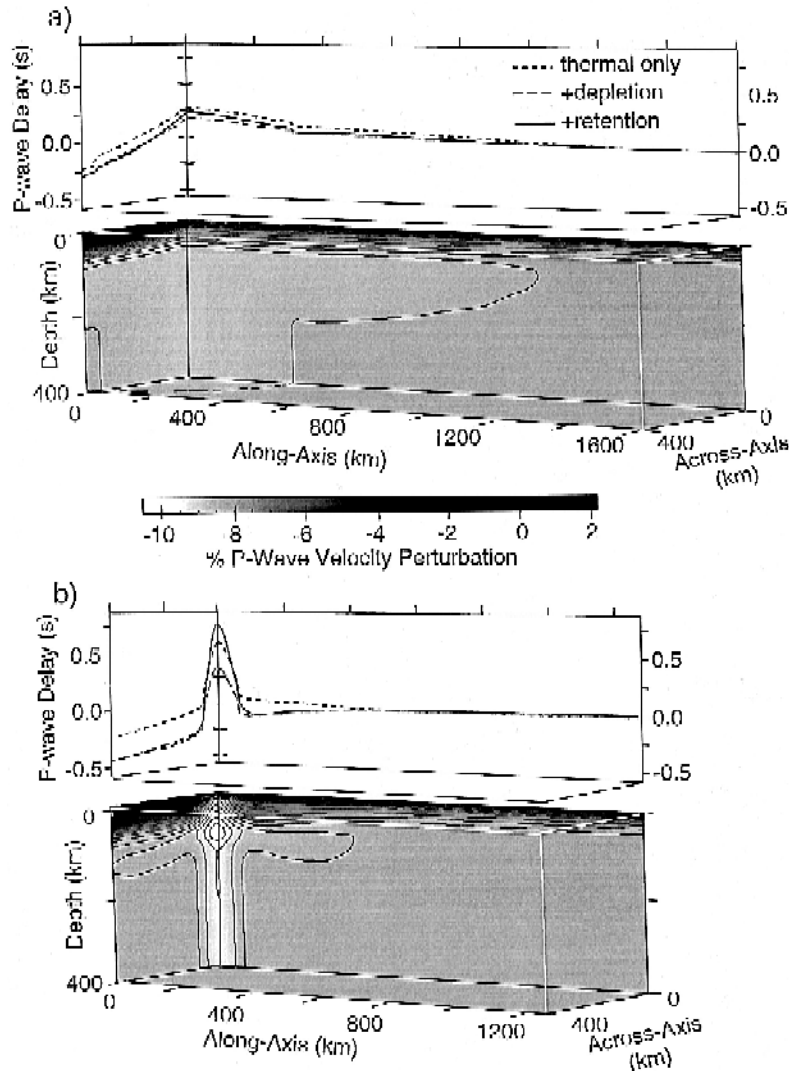

Fig. 9. (a) Lower diagram shows predicted P-wave velocity variations with contour interval of 0.5% for model Ice 1d (broad plume source) caused by the combined effects of temperature, melt depletion, and melt retention. Top panel illustrates the predicted P-wave travel-time delays, assuming vertically passing rays, for along-axial and across-axis profiles due to successively added mantle effects as labeled. (b) Same as (a) but for model Ice 2d (narrow plume source). The lowest velocity region occurs at depths 50–100 km due to the predicted high melt retention.

that, within most of the plume-affected portion of the ridge, very little mixing occurs between plume and ambient source material in the shallow mantle. Thus, if the gradients in $^{87}Sr/^{86}Sr$ away from Iceland reflect plume–MORB mixing, it most likely occurs deeper in the mantle, possibly by ambient mantle entrainment of the ascending plume (e.g. [42]).

5.5. Predictions of P-wave seismic velocity anomalies

Observations of compressional wave (P-wave) seismic travel-time variations and associated mantle P-wave velocity variations provide critical constraints on mantle properties beneath Iceland. To predict P-wave seismic velocity anomalies, we assume a reference P-wave velocity of 8 km/s, which decreases by $6.25 \times 10^{-3}\%$ for each 1°C increase in mantle temperature, increases by 0.1% for each 1% increase in depletion, and decreases by 1.25% for each 1% increase in pore volume [43]. We also predict P-wave travel-time residuals by calculating travel times of seismic rays passing vertically through the 400 km thickness of our mantle models.

The broad plume source model (Ice 1d) predicts a maximum decrease in P-wave velocity below the melting region of $\sim 0.5\%$ relative to the surrounding mantle. In the melting region, the predicted P-wave velocity anomaly diminishes because the velocity-enhancing effects of latent heat loss and melt depletion exceed the velocity-reducing effect of melt retention (Fig. 9a). The corresponding travel-time delay for vertically passing rays is predicted to be $+0.23$ s at the plume center and decrease to zero at an along-axis distance of ~ 1200 km. The contributions to travel-time delay above the plume center are $+0.25$ s from excess mantle temperature, -0.09 s from melt depletion, and $+0.07$ s from melt retention. Across the ridge-axis, lithospheric cooling dominates, resulting in a predicted travel-time difference of 0.5 s between the plume center and at an across-axis distance of 400 km. The broad plume source model thus predicts only a gradual decrease in travel-time delay across the ridge axis and even smaller variations along the ridge-axis.

In contrast, the narrow plume source of model Ice 2d predicts significantly larger amplitudes of P-wave

anomalies over a much narrower lateral extent. Below the melting zone, the 170°C plume temperature anomaly reduces calculated P-wave velocities by more than 1%. In the melt zone, however, the P-wave velocities are reduced to as much as 2% due to the 2.9% melt retention (Fig. 9b). Along the ridge-axis, the travel-time delay for vertically passing rays is predicted to be $+0.75$ s at the plume center and to decrease by 0.85 s within ~ 80 km. Approximately half of this travel-time residual is predicted to arise in the high-porosity melt zone in the shallow mantle. Across the ridge-axis, the additional effect of lithospheric cooling yields a predicted travel-time difference of 1 s within ~ 80 km of the plume center and a travel-time difference of 1.2 s over an across-axis distance of 400 km. Preliminary results of the ongoing ICEMELT experiment at Iceland have revealed azimuthal variations in P-wave travel times as high as 1 s within 100 km of the ridge axis [44], suggesting that the narrow plume source model better represents Iceland than does the broad plume source model.

6. Discussion

6.1. Importance of melting effects

The importance of melting effects on mantle flow, melt production, and surface observables are summarized in Fig. 10. Mantle melting generates appreciable effects on mantle properties; however, over the range of plume viscosities considered in our models, the effect of latent heat loss on mantle flow largely cancels the effects of depletion and retention buoyancy. As a result, the combined effects of these factors on mantle flow are small, as reflected in the small changes in the predicted values of $W(Q/U)^{-1/2}$ (Fig. 4 and Fig. 10). Similarly, when plume temperature anomalies are mild, as in the Ice 1 models, the melting-related factors have only second-order effects on upwelling rate, as reflected in small changes in the predicted crustal thickness (Fig. 10). When plume temperature anomalies are larger, however, as in the Ice 2 models, melt retention may enhance the predicted crustal thickness by 20% relative to calculations that do not include retention.
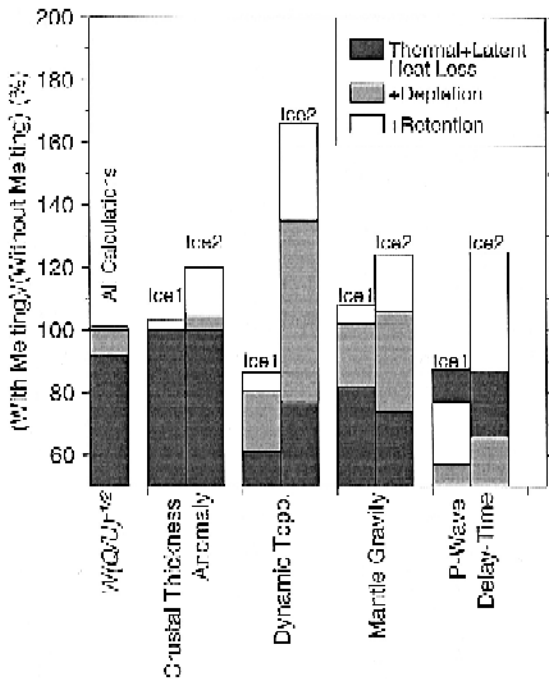
Fig. 10. Characteristic variables predicted by models with melting normalized by those predicted by models without melting. We choose the mean value of $W(Q/U)^{-1/2}$ for each experimental set and maximum value of along-axis variations for each of the other variables. Crustal thickness anomalies are normalized by calculations with thermal buoyancy and latent heat loss.

Contrasting with their mild influence on mantle flow, the melting-related factors have substantial effects on the predicted geophysical observables and these effects increase with increasing plume temperature (Fig. 10). For mantle contributions to topography and MBA, latent heat loss reduces the amplitudes of predicted anomalies by 20–40% relative to calculations without latent heat loss. Depletion buoyancy increases predicted mantle topographic anomalies and MBA by 10–65% relative to calculations without depletion, while retention buoyancy increases predicted anomalies by 5–25% relative to calculations without retention. Melting effects on P-wave delay-time are also important: latent heat loss decreases predicted delay-time by ∼ 13%, melt depletion decreases delay-time by 20–30%, but melt retention increases delay-time by 20–60%. It is thus important to consider melting effects on mantle properties when predicting geophysical observables.

6.2. Model uncertainties

Because melting-related factors do not affect significantly large-scale mantle flow, uncertainties associated with our melt calculations, such as the assumed batch melting [25], our choice of β values, and the melt porosity calculations, are likely to have only secondary effect on our estimates of plume source radius and temperature. By far the most important uncertainty in this regard is mantle rheology. The reference mantle viscosity η_o controls directly the rate of mantle upwelling in response to density variations (Eq. (9)). But, unfortunately, viscosity beneath ridges is not known to within one or even two orders of magnitude (e.g. [45]). One mechanism that may yield a substantially higher viscosity than that which we have assumed is dehydration at the onset of melting [45]. A higher melting zone viscosity, for example, would most likely require a greater temperature anomaly of the broad plume source model to explain the geophysical observations, or require a greater source radius and less along-axis melt redistribution of our narrow plume source model to explain the observations. Thus, because of the uncertainty of viscosity, our Iceland plume models are not unique. However, they do provide reasonable bounds on the plume source radius and temperature given the similarities between model predictions and the variety of geophysical and geochemical observations considered.

6.3. Plume volume flux estimates

It may still be possible to constraint plume volume flux independent of ambient viscosity based on the observed MBA and bathymetric anomaly widths and the theoretical relationship between flux and W (i.e. Eq. (13)). The use of Eq. (13) to infer plume volume flux is valid if the surface anomaly widths directly reflect the along-axis plume width in the mantle, which would be the case if along-axis melt migration is negligible, as assumed in the Ice 1 models. The flux required to match the along-axis MBA and bathymetric anomaly widths as predicted from model Ice 1d is 1.2×10^7 km^3/my. This flux, however, is several times larger than previous estimates of the Iceland plume of 2×10^6 km/my [46], 1.43×10^6 km/my [8], and 2.2×10^6 km/my [28].

If, on the other hand, along-axis melt migration is important, as suggested for the Ice 2 models, we cannot use Eq. (13) to constrain the Iceland plume volume flux independent of η_o. We must therefore rely on the fact that our melt production rate estimates are consistent with the total volume of observed excess crust as we did for the Ice 2 models. Indeed, model Ice 2d predicts a plume volume flux of 2.1×10^6 km^3/my which is more consistent with the above estimates of the previous studies. An intriguing new question arising from this narrow plume source model is, what specific mechanisms may allow melt generated beneath Iceland to migrate hundreds of kilometers along-axis? Possible evidence for such melt transport may include the V-shaped axial bathymetric highs propagating away from Iceland along the Reykjanes Ridge as first noted by Vogt [47] in 1971.

7. Conclusions

We have investigated the dynamics of mantle flow and melting of a ridge-centered plume using three-dimensional, variable-viscosity models with focus on three buoyancy sources: temperature, melt depletion, and melt retention. When all melting effects are considered, the relationship between along-axis plume width, W, plume volume flux, Q, full spreading rate, U, buoyancy number, B, and ambient/plume viscosity ratio, γ, is best parameterized by $W = 2.37(Q/U)^{1/2}(B\gamma)^{0.04}$. Calculations that include melting yield a similar relationship to those that do not include melting because of the competing effects of latent heat loss and depletion buoyancy. We propose two end-member models for the Iceland plume beneath the MAR. The broad plume source of radius = 300 km represents a low temperature ($\Delta T_p = 75°C$) and high flux ($Q = 1.2 \times 10^7$ km^3/my) end-member, while the narrow plume source of radius = 60 km represents a high temperature ($\Delta T_p = 170°C$) and low flux ($Q = 2.1 \times 10^6$ km^3/my) end-member. The broad plume source predicts successfully the observed along-axis variations in seismic crustal thickness, topography, and mantle Bouguer gravity anomalies; whereas the narrow source model predicts adequately the total excess crustal production rate (2.5×10^5 km^3/my) but requires extensive

melt migration and/or lower crustal ductile flow to occur over hundreds of kilometers along the MAR in order to explain the geophysical and geochemical observations. Our calculations predict that plume spreading away from the plume center is radially symmetric rather than channelled preferentially along the ridge axis. The elongated bathymetric swell along the Reykjanes Ridge can be explained by rapid off-axis subsidence due to lithospheric cooling superimposed on a broader hotspot swell. Both the broad and narrow plume source models predict very little mixing between the plume and MORB sources in the shallow mantle; hence, we suggest that mixing may occur deeper in the mantle, possibly due to entrainment of the isotopically depleted portion of the mantle by the rising mantle plume. Our narrow plume source model predicts seismic P-wave velocity variations more consistent with recent seismic observations beneath Iceland, suggesting that this model may better represent the Iceland plume.

References

[1] M.F. Coffin and O. Eldholm, Large igneous provinces: Crustal structure, dimensions, and external consequences, Rev. Geophys. 32, 1–36, 1994.

[2] W.J. Morgan, Convection plumes in the lower mantle, Nature 230, 42–43, 1971.

[3] P.R. Vogt, Evidence for global synchronism in mantle plume convection, and possible significance for geology, Nature 240, 338–342, 1972.

[4] J.-G. Schilling, Iceland mantle plume: Geochemical study of Reykjanes Ridge, Nature 242, 565–571, 1973.

[5] P.R. Vogt, Plumes, subaxial pipe flow, and topography along the mid-ocean ridge, Earth Planet. Sci. Lett. 29, 309–325, 1976.

[6] J.-G. Schilling, Upper mantle heterogeneities and dynamics, Nature 314, 62–67, 1985.

[7] J.-G. Schilling, G. Thompson, R. Kingsley and S. Humphris, Hotspot-migrating ridge interaction in the South Atlantic, Nature 313, 187–191, 1985.

[8] J.-G. Schilling, Fluxes and excess temperatures of mantle plumes inferred from their interaction with migrating mid-ocean ridges, Nature 352, 397–403, 1991.

[9] M.A. Feighner and M.A. Richards, The fluid dynamics of plume–ridge and plume–plate interactions: an experimental investigation, Earth Planet. Sci. Lett. 129, 171–182, 1995.

[10] M.A. Feighner, L.H. Kellogg and B.J. Travis, Numerical modeling of chemically buoyant mantle plumes at spreading ridges, Geophys. Res. Lett. 22, 715–718, 1995.

[11] N. Ribe, U.R. Christensen and J. Theissing, The dynamics of plume–ridge interaction, 1: Ridge-centered plumes, Earth Planet. Sci. Lett. 134, 155–168, 1995.

[12] E.R. Oxburgh and E.M. Parmentier, Compositional and density stratification in oceanic lithosphere—causes and consequences, J. Geol. Soc. London 133, 343–355, 1977.

[13] J.L. Ahern and D.L. Turcotte, Magma migration beneath an ocean ridge, Earth Planet. Sci. Lett. 45, 115–122, 1979.

[14] J. Phipps Morgan, Melt migration beneath mid-ocean spreading centers, Geophys. Res. Lett. 14, 1238–1241, 1987.

[15] D.R. Scott and D.J. Stevenson, A self-consistent model for melting, magma migration and buoyancy-driven circulation beneath mid-ocean ridges, J. Geophys. Res. 94, 2973–2988, 1989.

[16] J. Phipps Morgan, W.J. Morgan and E. Price, Hotspot melting generates both hotspot volcanism and a hotspot swell?, J. Geophys. Res. 100, 8045–8062, 1995.

[17] D.W. Sparks, E.M. Parmentier and J. Phipps Morgan, Three-dimensional mantle convection beneath a segmented spreading center: Implications for along-axis variations in crustal thickness and gravity, J. Geophys. Res. 98, 21,977–21,995, 1993.

[18] K. Jha, E.M. Parmentier and J. Phipps Morgan, The role of mantle depletion and melt-retention buoyancy in spreading-center segmentation, Earth Planet. Sci. Lett. 125, 221–234, 1994.

[19] D.L. Turcotte and J. Phipps Morgan, The physics of magma migration and mantle flow beneath a mid-ocean ridge, in: Mantle Flow and Melt Generation Beneath Mid-Ocean Ridges, J. Phipps Morgan, D.K. Blackman and J.M. Sinton, eds., pp. 155–182, AGU, Washington, D.C., 1992.

[20] C.W. Gable, Numerical models of plate tectonics and mantle convection in three dimensions, Ph.D. Thesis, Harvard Univ., 1989.

[21] C.W. Gable, R.J. O'Connel and B.J. Travis, Convection in three dimensions with surface plates: Generation of toroidal flow, J. Geophys. Res. 96, 8391–8405, 1991.

[22] U. Christensen, Convection with pressure- and temperature-dependent non-Newtonian rheology, Geophys. J.R. Astron. Soc. 77, 343–384, 1984.

[23] U. Christensen and H. Harder, 3-D convection with variable viscosity, Geophys. J. Int. 104, 213–226, 1991.

[24] F. Busse, U. Christensen, R. Clever, et al., 3D convection at infinite Prandtl number in Cartesian geometry — A benchmark comparison, Geophys. Astrophys. Fluid Dynam. 75, 39–59, 1993.

[25] D. McKenzie and M.J. Bickle, The volume and composition of melt generated by extension of the lithosphere, J. Petrol. 29, 625–679, 1988.

[26] K.W.W. Sims and D.J. DePaolo, Porosity of the melting zone beneath Hawaii and mid-ocean ridges: Inferences from ^{238}U–^{230}Th–^{226}Ra disequilibria, in: 6th V.M. Goldschmidt Conf., Heidelberg, Germany, 1996.

[27] G. Ito, J. Lin and R.S. Detrick, The effects of near-ridge hot spots on mid-ocean ridge density and temperature structure from analysis of gravity and bathymetry: Results from the Galapagos, Azores, and Iceland, EOS Trans. Am. Geophys. Union Spring Meet. Suppl. 75, 335, 1994.

[28] G. Ito and J. Lin, Oceanic spreading center–hotspot interactions: Constraints from along-isochron bathymetric and gravity anomalies, Geology 23, 657–660, 1995.

[29] B.-Y. Kuo and D.W. Forsyth, Gravity anomalies of the ridge–transform system in the South Atlantic between 31° and 34.5°S: Upwelling centers and variations in crustal thickness, Mar. Geophys. Res. 10, 205–232, 1988.

[30] J. Lin, G.M. Purdy, H. Schouten, J.-C. Sempéré and C. Zervas, Evidence from gravity data for focused magmatic accretion along the Mid-Atlantic Ridge, Nature 344, 627–632, 1990.

[31] G. Ito and J. Lin, Mantle temperature anomalies along the present and paleoaxes of the Galápagos Spreading Center as inferred from gravity analyses, J. Geophys. Res. 100, 3733–3745, 1995.

[32] W. Menke and D. Sparks, Crustal accretion model for Iceland predicts 'cold' crust, Geophys. Res. Lett. 22, 1673–1676, 1995.

[33] R.S. White, J.W. Bown and J.R. Smallwood, The temperature of the Iceland plume and origin of outward propagating V-shaped ridges, J. Geol. Soc. London 152, 1039–1045, 1995.

[34] B. Parsons and J.G. Sclater, An analysis of the variation of ocean floor bathymetry and heat flow with age, J. Geophys. Res. 82, 803–827, 1977.

[35] R.L. Parker, The rapid calculation of potential anomalies, Geophys. J.R. Astron. Soc. 31, 447–455, 1973.

[36] C. DeMets, R.G. Gordon, D.F. Argus and S. Stein, Effect of recent revisions to the geomagnetic reversal time scale on estimates of current plate motions, Geophys. Res. Lett. 21, 2191–2194, 1994.

[37] J.R. Smallwood, R.S. White and T.A. Minshull, Seafloor spreading in the presence of the Iceland plume: the structure of the Reykjanes Ridge at 61°40′N, J. Geol. Soc. London 152, 1023–1029, 1995.

[38] P.D. Clift, J. Turner and ODP Leg 152 Scientific Party, Dynamic support by the Iceland plume and its effect on the subsidence of the northern Atlantic margins, J. Geol. Soc. London 152, 935–942, 1995.

[39] D. McKenzie, The generation and compaction of partially molten rock, J. Petrol. 25, 713–765, 1984.

[40] W.R. Buck, Along-axis crustal flow and ridge topographic segmentation, EOS Trans. Am. Geophys. Union Spring Meet. Suppl. 77, 276, 1996.

[41] J.-G. Schilling, Geochemical and isotopic variation along the Mid-Atlantic Ridge axis from 79°N to 0°N, in: The Geology of North America, P.R. Vogt and B.E. Tucholke, eds., pp. 137–156, GSA, Boulder, Colo., 1986.

[42] E.H. Hauri, J.A. Whitehead and S.R. Hart, Fluid dynamics and geochemical aspects of entrainment in mantle plumes, J. Geophys. Res. 99, 24,275–24,300, 1994.

[43] E.D. Humphreys and K.G. Dueker, Physical state of the western U.S. upper mantle, J. Geophys. Res. 99, 9635–9650, 1994.

[44] I.T. Bjarnason, C.J. Wolfe and S.C. Solomon, Initial results from the ICEMELT experiment: Body-wave delay times and shear-wave splitting across Iceland, Geophys. Res. Lett. 23, 459–462, 1996.

[45] G. Hirth and D.L. Kohlstedt, Water in the oceanic upper mantle: Implications for rheology, melt extraction, and the evolution of the lithosphere, Earth Planet. Sci. Lett., in press, 1996.

[46] N.H. Sleep, Hotspots and mantle plumes: Some phenomenology, J. Geophys. Res. 95, 6715–6736, 1990.

[47] P.R. Vogt, Asthenosphere motion recorded by the by the ocean floor south of Iceland, Earth Planet. Sci. Lett. 13, 153–160, 1971.

[48] P. Wessel and W.H.F. Smith, New version of the Generic Mapping Tools released, EOS Trans. Am. Geophys. Union 76, 329, 1995.

[49] M. Spiegelman, Geochemical consequences of melt transport in 2-D: The sensitivity of trace elements to mantle dynamics, Earth Planet. Sci. Lett. 139, 115–132, 1996.